Modelling of Cavity Nucleation, Early-stage Growth and Sintering in Polycrystal under Creep-fatigue Interaction

J.-D. Hu[1], C.-J. Liu[1], Fuzhen Xuan[1], and Bo Chen[2]

[1]East China University of Science and Technology School of Mechanical Engineering and Power Engineering
[2]University of Leicester

June 13, 2021

Abstract

A mechanistic based cavitation model that considers nucleation, early-stage growth and sintering under creep-fatigue interaction is proposed. The number density of cavities ρ and their evolution during multi-cycle creep-fatigue loading are predicted. Both the cavity nucleation and early-stage growth rates, controlled by grain boundary (GB) sliding mechanism during the tension phase, are formulised as a function of local normal stress σ_{n}. The cavity sintering that occurs during the compression phase is described as a function of σ_{n}, but the mechanism switches to the unconstrained GB diffusion. By examining various load waveform parameters, results provide important insights into experimental design of studying the creep-dominated cavitation process under creep-fatigue interaction. First, creep-fatigue test with initial compression will promote higher ρ value compared to that with initial tension, if the unbalanced stress hold time in favour of tension is satisfied. Second, the ρ value does not have a monotonic dependence on either the compressive hold time or stress level, because of their competing effect on nucleation and sintering. Third, the optimum value of stress variation rate exists in terms of obtaining the highest ρ value due to sintering effect.

Modelling of Cavity Nucleation, Early-stage Growth and Sintering in Polycrystal under Creep-fatigue Interaction

J.-D. Hu[a,b,]11Present Address: Shanghai Nuclear Engineering Research and Design Institute, Shanghai 200233, China[*], C.-J. Liu[a], F.-Z. Xuan[a], B. Chen[b**]

[a]*Key Laboratory of Pressure Systems and Safety, Ministry of Education, School of Mechanical and Power Engineering, East China University of Science and Technology, Shanghai 200237, China*

[b]*School of Engineering, University of Leicester, Leicester, LE1 7RH, UK*

*Corresponding authors. E-mail address: **jh788@leicester.ac.uk*;

***bo.chen@leicester.ac.uk*

Abstract

A mechanistic based cavitation model that considers nucleation, early-stage growth and sintering under creep-fatigue interaction is proposed. The number density of cavities ρ and their evolution during multi-cycle creep-fatigue loading are predicted. Both the cavity nucleation and early-stage growth rates, controlled by grain boundary (GB) sliding mechanism during the tension phase, are formulised as a function of local normal stress σ_{n}. The cavity sintering that occurs during the compression phase is described as a function of σ_{n}, but the mechanism switches to the unconstrained GB diffusion. By examining various load waveform parameters, results provide important insights into experimental design of studying the creep-dominated

cavitation process under creep-fatigue interaction. First, creep-fatigue test with initial compression will promote higher ρ value compared to that with initial tension, if the unbalanced stress hold time in favour of tension is satisfied. Second, the ρ value does not have a monotonic dependence on either the compressive hold time or stress level, because of their competing effect on nucleation and sintering. Third, the optimum value of stress variation rate exists in terms of obtaining the highestρ value due to sintering effect.

Keywords: Creep; Cavity; Viscoplastic; Analytic solutions; Cavity sintering

1. Introduction

Creep-dominated creep-fatigue interaction is a long-term material failure mode that involves cyclic loading [1]. Lack of fundamental understanding on this topic prevents us to commercialise the Generation IV high-temperature nuclear power plants with a design life of 60 years [2]. Although the mechanistic-based descriptions of cavity nucleation, growth and coalescence under creep have been established [3], little attempt has been made to reveal the mechanism of cavity nucleation and its early-stage radius change under creep-fatigue interaction [4, 5].

The empirical relationship between cavity nucleation rate under creep and Monkman-Grant constant has been established by Davanas[6], providing a good agreement with experimental data. But it is unclear about its suitability for creep-fatigue interaction. Cavitation under fatigue is known to be different from that under creep, in a sense that fatigue induced cavities are smaller in size but higher in their number density [5]. There are creep-fatigue lifetime prediction models that consider the creep cavitation mechanism, e.g. Nam [7]. However, the model cannot explain the positive relationship between the cavity nucleation and tensile hold time [8]. Recent work by Wen, Srivastava[9] and Barbera, Chen [10] used creep damage models to predict crack growth rate under creep-fatigue, by incorporating the late-stage cavity growth. However, they did not consider the physical process of cavity nucleation or early-stage growth.

Moreover, little knowledge has been gained regarding the cavity sintering. Compressive loading can cause the nucleated creep cavities shrink in radius and forces them to be removed completely under some circumstances [11, 12]. This means that their number density after certain number of cycles is not the simple sum of nucleated cavities from each cycle. To the best of the authors' knowledge, creep cavitation model considering both the nucleation and sintering events under creep-fatigue interaction does not exist so far.

The mechanism of cavity nucleation was initially proposed by Greenwood[13], and developed further by Raj and Ashby[14]. It has been accepted that vacancies agglomerate and form stable nuclei assisted by local normal stress. The local normal stress can be significantly higher than the far-field stress[15]. One of the causes is grain boundary (GB) sliding induced stress concentration. Extensive cavitation was found in copper bi-crystals which had been subjected to pre-strain in favour of GB sliding followed by creep loading [16, 17]. Min and Raj[18] proposed a model to predict the local normal stress under creep-fatigue loading based on the GB sliding mechanism. By considering the creep effect on local normal stress, our model is capable of predicting the cavity nucleation under one-cycle creep-fatigue [19].

Modelling the early-stage radius change is key to understanding the sintering process under creep-fatigue. Note that sintering shares a high degree of commonality with the cavity growth. The classical growth models were established under either or both of vacancy diffusion and matrix deformation (Cocks [20,] Cocks and Ashby[21,] Needleman and Rice [22,] Chuang, Kagawa [23,] Chen and Argon [24]), and the growth rate is controlled by the far-field stress. Nevertheless, these models might not be suitable for the early-stage growth. First, the radius of nucleated cavities (~5 nm) is much smaller than those commonly defined 'small' cavities (~1 μm)[3]. This indicates that the vacancy flow near the cavities is highly sensitive to the local normal stress[25]. Second, the cavity growth mechanism map[26] does not consider the role of GB sliding on the early-stage growth, despite its importance [25].

In this paper, the number density of cavities and their time evolution during multi-cycle creep-fatigue loading are modelled. The stress-controlled load waveform is considered because a higher creep damage would be generated in comparison with the strain-controlled one[27, 28]. Type 316 stainless steel is selected for twofold reasons: material parameters are available [18, 29-31] and its wide application to the power generation industry[2, 29].

2. Modelling approach

2.1 Theoretical modelling

Modelling cavitation under creep-fatigue contains two parts. The first part focuses on describing the relationship between the applied stress and local normal stress, and the cavity nucleation governed by vacancy accumulation. The second part concerns about the radius change of nucleated cavities during creep-fatigue loading. These two parts are integrated through a numerical framework to give the final prediction to the number density of cavities. The governing equations are described below.

The rate of cavity nucleation () on the particles at GB can be described as [14]:

where Ω is the atomic volume and k is the Boltzmann constant. δD_{B} is the GB thickness multiplied by its self-diffusion coefficient. γ is the free surface energy.F_{v} is a shape factor related to the cavity volume, and it has a value of 0.1585 for cavity nucleation at the top of GB particles [14]. ρ_{max} is the maximum number density of potential nucleation sites, and its value can be worked out through the relation of [32], by assuming that grain has an idealised hexagonal shape. $f_{b}$is the area fraction of GB particles, is their average radius (in μm), and d is the grain size (in μm). A coefficient of 10^6 appears due to the unit conversion when expressing the number density of cavities in mm^{-2}.

The cavity nucleation rate in Eq. depends on three variables: number density of nucleated cavities, local normal stress and temperature, symbolised as ρ , σ_{n} and T , respectively. Accordingly, the relationship between the local normal stress and applied shear stress is formulised as follow:

where , and are the applied shear stress, its change rate and the local normal stress at time t . The derivation of Eq. is described in Appendix A. is the local normal stress at time $t+\Delta t$. Note Δt is the time interval chosen for the numerical computation that will be described in Section 2.3. τ is time constant defined as:

where $_{b}$ is the damping coefficient of GB sliding. k_{e} is the elastic modulus, defined as$G/[0.57d\ (1\text{-}v)]$. is the transient creep damping coefficient that has a form of $_{p}/[\sigma_{s}\text{-}f_{b}\sigma_{n}]^{n-1}$.$G$ and v are shear modulus and Poisson's ratio. $_{p}$ is the reciprocal of pre-exponential factor and n is the exponent in the Norton power-law creep equation. More details about the cavity nucleation model can be found in Hu, Xuan[19].

To obtain the actual size of the nucleated cavities, the radius change rate needs to be determined during the subsequent loadings. For cavity growth, Chen [25] pointed out that GB sliding played an important role in the early-stage growth. The transient GB sliding activity could immediately wedge open the supercritical nuclei along the particles [33]. According to this 'crack sharpening' mechanism, the cavity tip velocity is limited by surface diffusion[3].

Fig. 1a shows a schematic diagram of the cavity nucleation and early-stage growth assisted by GB sliding with a rate of . Because of insufficient surface diffusion, the nucleated cavity tends to form an irregular crack-like shape. This implies that the growth rate is independent of the cavity radius, given that the process is limited by the vacancy diffusion rate near the cavity tip. Based on the work of Chuang, Kagawa [23], equations were formulised by Nix, Yu [34] to describe cavity growth rate controlled by the vacancy surface diffusion under low and high stresses:

where D_S is the surface diffusion coefficient. δ_S is the width of surface diffusion, which is related to atom volume Ω, through $\delta_S = \Omega^{1/3}$. b is the limiting cavity radius, equalling the half of average cavity spacing, $\lambda/2$ [23]. λ is the average distance between two nucleation sites, and its value can be estimated as below for an idealised hexagonal grain shape:

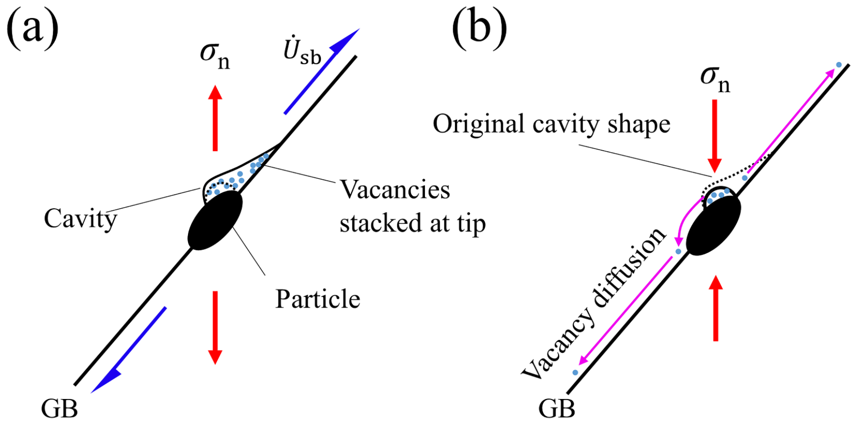

Fig. 1: Schematic diagrams of a cavity that (a) grows by the surface diffusion limited GB sliding; (b) shrinks by the unconstrained GB diffusion.

In the growth model [34], the cavity has been assumed to have a crack-like shape, Fig. 1a. The growth process is driven by the accumulation of vacancies at the cavity tip, leading to the phenomenon similar to a crack-tip continuous extension. Meanwhile, the surface diffusion is not very much faster than GB diffusion under low stress, while the surface diffusivity becomes much higher than that of GB under high stress. Refer to Appendix B for the derivation of stress level that separates the two conditions.

The reason for ignoring the creep effect on the early-stage growth can be justified as follows. The growth mechanism map proposed by Miller, Hamm [26] informs that the cavity radius change is controlled by unconstrained GB diffusion when the ratio of cavity spacing (λ) to its diameter ($2r$) is greater than 10. In the case of early-stage cavitation, the value of $\lambda/2r$ falls into the range of 200 to 3000, given that the value range of r is 3 to 5 nm[3] and that of λ is 1 to 10 µm [23]. Therefore, the unconstrained GB diffusion is the rate-limiting factor for the early-stage growth.

Because of the analogy of shrinkage to growth, shrinkage occurs by the GB vacancy diffusion that pushes vacancies out of the cavity under the compressive σ_n. The reversed direction of GB sliding, coupled with the reduced sharpness of the cavity tip, causes a more uniform distribution of vacancies within the cavity, as shown in Fig. 1b. Since the vacancies are no longer concentrated at the tip, more surface areas become the diffusional interface. Ultimately, the cavity shape changes back to sphere, that is the equilibrium shape when the surface diffusion rate is fast enough [23].

To calculate the shrinkage rate, equation proposed by Riedel[35] for cavity growth under the unconstrained GB diffusion is adapted:

When the cavity radius r becomes larger than $\lambda/4.24$, is set to zero to prevent the unrealistic positive value under compression. This upper limit value has been used to define the largest cavity size. The assumption behind the Riedel model is that cavity is not perfectly spherical, which aligns very well with the considered crack-like cavities in the present work. If the cavity radius r becomes less than the critical nuclei size defined by the value of $2\gamma/\sigma_n$ [14], cavities are considered as sintered [12, 36].

2.2 Material parameters and temperature effect

Except for the surface diffusion factor D_{S}, all the material parameters have been sourced from the authoritative literature listed in Table 1. D_{S} values in the temperature range of 500-600 @C are not available; hence the diffusivity ratio of$\delta_{\mathrm{S}} D_{\mathrm{S}}/\delta\Delta_{\mathrm{B}}$=0.001 has been used for calculations. This meets the criterion of$\delta_{\mathrm{S}} D_{\mathrm{S}}/\delta\Delta_{\mathrm{B}}$<<1 for a crack-like cavity [34]. Justification of theD_{S} value selection through a sensitivity study is described in Appendix B. In this context, our model has been established based on the state-of-the-art mechanistic understanding of cavitation and the prediction results are reliable (no approximation or extrapolation).

Creep database for Type 316H stainless steel [29] has been used to derive the power-law creep related parameters (1/ $_{\mathrm{p}}$ and n, Table 1) for two reasons. First, this material was subjected to 65,015 h in service at temperatures between 490 and 530 @C, prior to creep testing [37]. Thus, it is unlikely that GB particle evolution occurs during the test (hence a fixed f_{b} value). Second, the operating pressure of less than 20 MPa would be too low to generate any noticeable creep cavities in this ex-service material, and hence no need to consider pre-existing cavities in our calculations. Note that the maximum allowable carbon content for Type 316 stainless steel is <0.08 wt.% according to [38]. This means that the chosen material with a carbon content of 0.06 wt.%[39] falls into the category of Type 316 stainless steel.

Table 1. Material parameters in the proposed cavity nucleation and sintering model for Type 316 stainless steel

Parameter	Symbol	Value	Unit	Temperatu
Average radius of the particle at GB		1.0	µm	-
Average size of grains	d	40	µm	-
Shear modulus	G	7.6×10^{10}	Pa	-
Poisson's ratio	v	0.31	-	-
Atom volume	Ω	1.21×10^{-29}	m^3	-
Area fraction of the particles	f_{b}	0.2	-	-
Shape factor related to the cavity volume	F_{v}	0.1585	-	-
Free surface formation energy	γ	0.80	$J.m^{-2}$	-
Boltzmann constant	k	1.3806×10^{-23}	$J.K^{-1}$	-
Gas constant	R	8.314	$J.mole^{-1}.K^{-1}$	-
GB diffusion activation energy	Q_c	167×10^3	$J.mole^{-1}$	-
GB thickness multiplied by its self-diffusion coefficient	$\delta\Delta_{\mathrm{B}}$	$2.0\times10^{-13}\exp(-Q_c/RT)$	$m^3.s^{-1}$	-
Free surface diffusion coefficient*	D_{S}	$9.0\times10^{-7}\exp(-167\times10^3/RT)$	$m^2.s^{-1}$	500-600
Creep exponent	n	11.83	-	500-600
Pre-exponential factor	$1/_{\mathrm{p}}$	2.199×10^{-32}	$h^{-1}.MPa^{-n}$	500
		8.754×10^{-32}		525
		6.489×10^{-31}		550
		3.035×10^{-30}		575
		2.005×10^{-29}		600

*Note: Value has been calculated through the relation of$\delta_{\mathrm{S}} D_{\mathrm{S}}/\delta\Delta_{\mathrm{B}}$=0.001.

Fig. 2a shows the relationship between σ_{n} and cavity growth rate at three different temperatures of 500/550/600 @C, as predicted by Eq.(4). The cavity growth rate increases by one order of magnitude with temperature increasing from 500 to 600 @C. However, the transition value of σ_{n} (~400 MPa), which differentiates the cavity growth mechanism under low and high stresses, is not affected by the temperature. This is as expected because the GB diffusion has the same activation energy as the surface diffusion (Table 1). Effects of the radius r andσ_{n} on cavity shrinkage rate are shown in a contour plot of Fig. 2b, as predicted by Eq.(6). Different colours signify temperatures of 500/550/600 @C, respectively. For each temperature, the contour curves with the largest value are always towards the top left, indicating that a higher compressive stressσ_{n} or smaller cavity radius r results in a higher shrinkage rate. By comparing different coloured curves with the same value, the shrinkage rate is found to be positively correlated with temperatures.

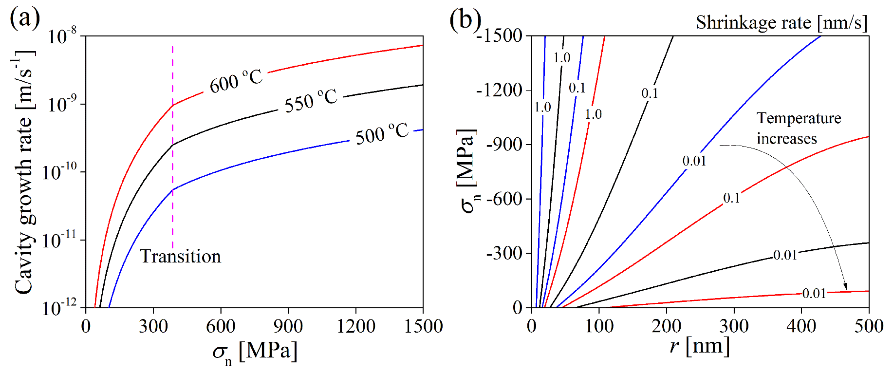

Fig. 2: Effects of: (a) local normal stress σ_{n} on cavity growth rate; (b) cavity radius r andσ_{n} on shrinkage rate at 500 @C (blue), 550 @C (black) and 600 @C (red).

2.3 Numerical implementation

Numerical computation of the cavity number density during creep-fatigue was performed in a sectionalised manner. Let's consider a time section$i$, the time period starts from $(i\text{ -}1)\Delta t$ and ends at$i\ \Delta t$, and a group of cavities can be nucleated during the time interval Δt . This group of cavities are named as 'cavities of the i -th group'. All the cavities belonging to this group would have the same radius and hence they are assigned as the nucleated cavities within the time section i . The number density of cavities of the i -th group is marked asρ_ι , with its value equalling the product of nucleation rate and Δt . The cavity is considered as nucleated when its radius reaches the value of $2\gamma/\sigma_{\text{n}}$, and we assign the symbol$^0 r_i$ representing the critical nucleation radius.

Since the growth rate is related to their radius, the cavities of$i$ -th group would have their characteristic rate at later time sections. For a time section k ($k > i$), the cavity radius of the i -th group, symbolised as$^{k\text{ -}i}\ r_i$, can be worked out:

where is the growth rate at time section $j(j > i$). This implies that cavities of the$i$ -th group are considered as sintered, when the value of$^{k\text{ -}i}\ r_i$ is less than that of $^0 r_i$. Thus, the sintered condition is defined as:

A flag variable (e.g. Flag(i) for cavities of the i -th group) is assigned to each cavity group as soon as cavities are nucleated, and this will be updated at following time sections. The flag value of 1 means that this group of cavities still exists, whilst 0 means that it is as sintered.

The number density of cavities ρ (k) at the end of time section k ($k > i$) after taking sintering into account can be formulised as:

where ρ_κ is the number density of cavities nucleated within the time section k . The cavitated GB area fraction f (k) at the end of time section k can be then derived with the assumption of idealised hexagonal grain shape:

The coefficient of 10^6 has been generated due to the unit conversion that involves the parameters of ρ in mm^{-2}, r in µm, and d in µm.

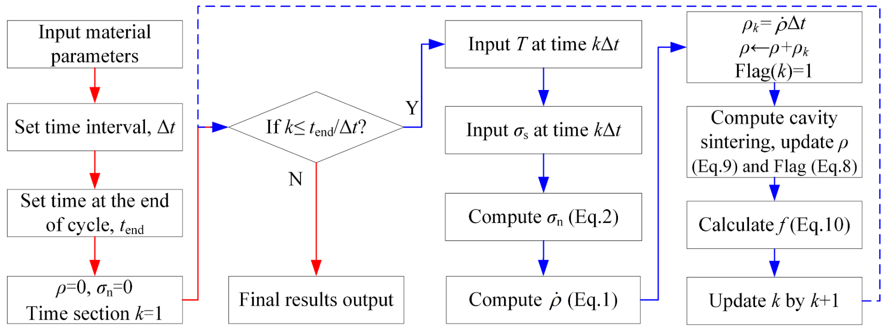

Fig. 3: Overall flow chart of the numerical computation

The numerical algorithm is depicted in Fig. 3 using a flow chart. First, the material parameters in Table 1 are read by our self-written MATLAB script. Afterwards, Δt is read from input, ρ andσ $_n$ are set to zero, and the iteration begins at the time section k =1. Within each iteration, T andσ $_s$ at time k Δt are read first, thenσ $_n$ can be calculated by Eq.. Next, the nucleation rate is computed by Eq., from which the initial ρ that does not consider the sintering effect can be worked out. After this step, the script enters into the sintering module, which is ruled by Eq.. Note that the flag variable will be updated with a value of 0 if the considered cavity group is found to be as sintered using the criterion given in Eq.. Afterwards, the cavitated GB area fraction f can be calculated by Eq.. At the end of each iteration, time section $k$is updated by k +1, and a new iteration begins. Refer to Appendix C for the limited numerical error generated by using the forward Euler method together with Δt =0.5 s.

3. Model prediction

3.1 Key outputs

A typical load waveform in stress-controlled creep-fatigue with initial compression under σ $_s$[?][-150, 150] MPa and$T$ =550 @C is shown in Fig. 4. The first cycle is presented for illustration purpose, and the following cycles are the same. It consists of a pre-compressive stress hold for a period t $_c$and a tensile stress hold t $_t$. The magnitude of stress applied during compression is designated as $\Delta\sigma$ $_c$, and the stress applied during tension is $\Delta\sigma$ $_t$. The stress variation rate during load reversal is constant, symbolised as . Table 2 summarises the default value for load waveform parameters and test temperature. They are used to elaborate the key model outputs. A total number of 50 cycles have been calculated.

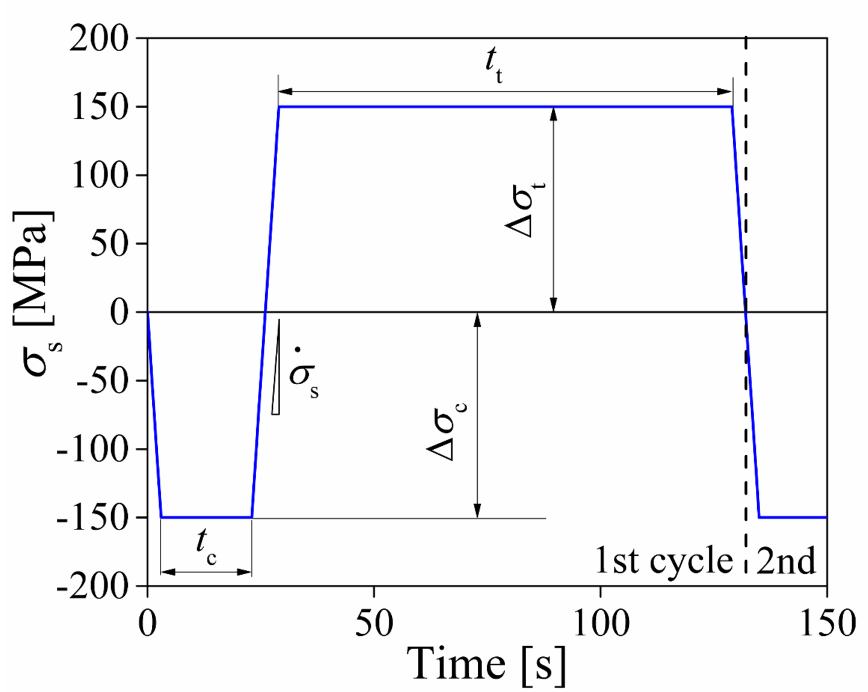

Fig. 4: A typical stress-controlled creep-fatigue load waveform

Table 2. Load waveform parameters and temperature in their default values

Parameters	Default value	Units
t_c	20	s
t_t	100	s
$\Delta\sigma_c$	150	MPa
$\Delta\sigma_t$	150	MPa
	50	MPa.s^{-1}
T	550	@C

Fig. 5a shows the model predicted σ_n as a function of the elapsed time/cycle. The maximumσ_n in each cycle is the sum of the relaxedσ_n in pre-compression and the increment ofσ_n induced by the load reversal. The maximumσ_n starts from a value of 761 MPa in the 1st cycle, and then decreases cycle by cycle. After 40 cycles, the maximumσ_n reaches its steady state with a value of 310 MPa, as highlighted by the hatched region in Fig. 5a. The evolution ofσ_n during the 1st cycle is shown in Fig. 5b, where the magnitude change due to the load reversal from compression to tension appears to be the same as that from tension to compression. In addition, the inset shows that the magnitude of relaxedσ_n in tensile hold (54 MPa) is larger than that in compressive hold (11 MPa). This stress difference is caused by the longer tensile hold time t_t than the compressive time t_c. Thus, the net $\sigma_n$change during the non-saturation cycle is negative (e.g. -42 MPa in the 1st cycle), leading to gradually decreased maximum value ofσ_n (Fig. 5a).

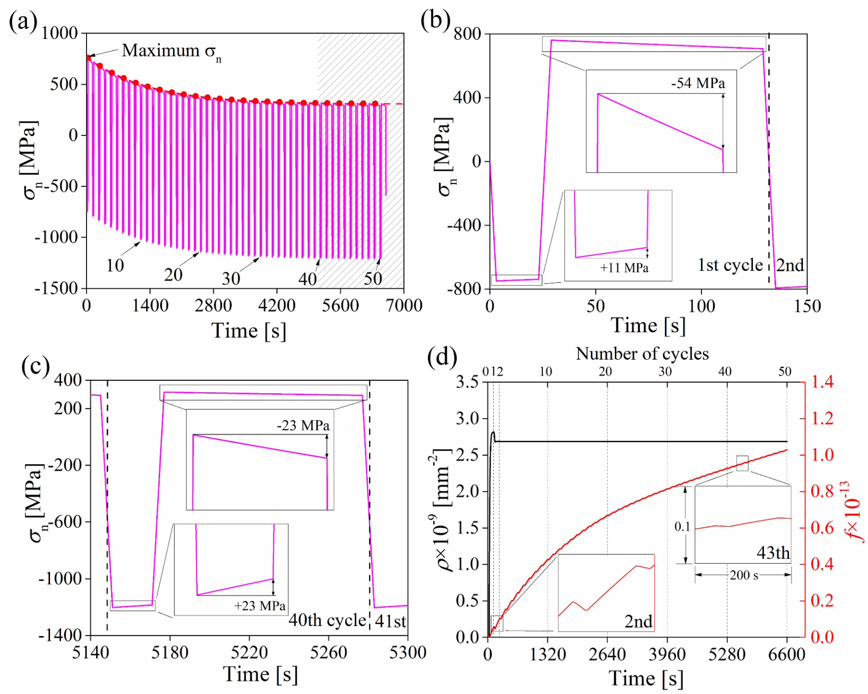

Fig. 5: Predicted time evolution curves of (a) the local normal stressσ_{n}; (b) σ_{n} in the 1st cycle; (c) σ_{n} in the 40th cycle (d) the number density of cavities ρ and cavitated GB fraction f .

When cyclic loading continues, the magnitude of relaxedσ_{n} in tensile hold decreases, whereas that in compressive hold increases. This is as expected because Eq.(2) includes an exponential decay function, indicating that an increased initial stress level would cause a faster stress relaxation over a fixed period of time. When the steady state is reached, the magnitude of relaxedσ_{n} in the tensile and compressive holds becomes identical. This can be clearly seen in Fig. 5c for the 40th cycle, where the tensile and compressive holds introduce 23 MPa stress relaxation, respectively. This means that the net stress change is 0 MPa in the steady state, being consistent with the observation in Fig. 5a.

Since nucleation rate is highly sensitive to σ_{n}, the maximum σ_{n} is key to cavity nucleation (i.e. the number density of cavities ρ). The model predicted ρevolution as well as cavitated GB fraction f during 50 cycles of creep-fatigue loading are shown in Fig. 5d. The ρ curve in black shows that most of the cavities are nucleated in the tensile hold of the 1st cycle, while the following compressive hold contributes to the major part of cavity sintering. After the first two cycles, the change inρ becomes negligible. By comparison, the f curve in red with its value read from the right axis (Fig. 5d) shows an overall increasing trend. This implies that the increased f value in later creep-fatigue cycles is most likely related to the cavity growth rather than the nucleation of new cavities.

To show this more evidently, two enlarged views of the f curve exhibiting a zigzag shape are highlighted in Fig. 5d. The zigzag shape can be explained by the fact that cavities nucleate and grow up when$\sigma_{\text{n}}>0$, and they shrink whenσ_{n}[?]0. The zigzag characteristic is more noticeable in the 2nd cycle than the 43th cycle, indicating that the cavity radius change rate reduces with the cycling. This implies that the cavity sintering is less likely to occur in the later cycles of creep-fatigue loading under the present waveform condition (i.e. $t_{\text{t}}>t_{\text{c}}$ in Fig. 4). Since the model predicts that the later creep-fatigue cycles neither nucleate many cavities (black curve in Fig. 5d) nor cause the already nucleated cavities to be sintered (red curve in Fig. 5d), it is appropriate to reduce fatigue cycles from 50 to 10 to save the computational cost.

In the work by Min and Raj [18], one purpose-designed creep-fatigue cycle at 625 @C was employed to create the increased fatigue crack growth rate from 0.05 to 0.17 mm/cycle on the Type 316 stainless steel. This specific load-waveform included a 15 mins stress hold under compression (-382 MPa), followed by a rapid load reversal from compression to tension (382 MPa) with a strain rate of 2×10^{-4} s^{-1}, and then applying a 1 hr stress hold under tension. The cavitation damage at grain boundaries was responsible for the increased crack growth rate. They further showed that imposing more than one fatigue cycle could not generate a further increase in the crack growth rate. Therefore, our model prediction in terms of the importance of the 1st fatigue cycle agrees with the experimental observation.

According to the predicted σ_n with a magnitude of 761 MPa (for a tensile hold stress $\Delta\sigma_t$ of 160 MPa in Fig. 5a) in the present work, the cavity nucleation rate would be $2.1\times10^{-10}mm^{-2}.s^{-1}$. When the magnitude of$\sigma_n$ increases to 1016 MPa, by applying a higher tensile stress hold of 200 MPa, the nucleation rate would change to 4.0×10^{-1} $mm^{-2}.s^{-1}$. Recall the work by Raj (1978), the predicted cavity nucleation rate was found to vary from 10^{14} to $10^{-16}mm^{-2}.s^{-1}$, if the local normal stressσ_n is decreased by an order of magnitude from 10^3 MPa to 10^2 MPa. Thus, our model prediction regarding the nucleation rate is as expected. It is well recognised (e.g. Evans [15]) that cavity nucleation under the GB sliding mechanism would require a high stress concentration (in the order of 10^3 to 10^4 MPa) particularly associated with the classical nucleation theory. Also, the nucleation rate (and cavity density) is strongly dependent on the material parameters [19, 40].

In this context, it is the predicted trend, rather than the specific value of cavity number density, that provides an important but missing guideline in terms of optimising the load-waveform design to produce more creep cavitation damage with reduced creep-fatigue experimental cost.

3.2 Effect of loading sequence

Creep-fatigue test can start either with the initial compression or tension. Fig. 6a compares these two loading sequences in terms of theσ_n evolution. The load waveform parameters and temperature used here are the same as that listed in Table 2, i.e.$t_t>t_c$. It can be seen that the test with initial compression has a higher maximumσ_n than that with initial tension. This is because the pre-compression period can relax theσ_n, contributing to the higher maximumσ_n in the tension phase. The difference of maximum σ_n between the two loading conditions is 12 MPa, which is in line with the relatively shortt_c of 20 s. The number density of cavitiesρ after 10 cycles was calculated as $2.6\times10^{-9}mm^{-2}$ for the test with initial compression, which is approximately one order of magnitude higher than that with initial tension ($\rho=4.9\times10^{-10}$ mm^{-2}), Fig. 6b.

Now let's consider a completely different scenario in which the compressive hold is prolonged, i.e.$t_c>t_t$. To this end, the σ_n evolution for a creep-fatigue loading with t_t=20 s andt_c=100 s was calculated. The test with initial compression is compared with that with initial tension. For both cases, the σ_n increases cycle by cycle, and the maximumσ_n appears at the last cycle, Fig. 6c. The test with initial compression has a higher maximum $\sigma_n$than that with initial tension. At the 1st cycle, the stress difference is 54 MPa, reducing to 23 MPa at the 10th cycle (the last cycle of calculation). This implies that the maximum $\sigma_n$difference between the two loading conditions will eventually diminish to 0 MPa if the cyclic loading continues.

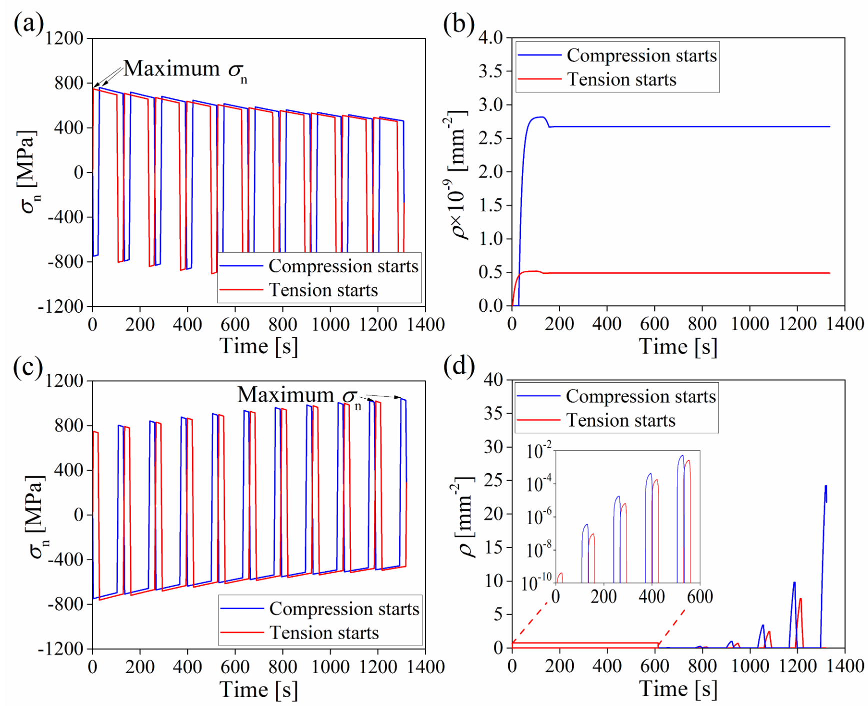

Fig. 6: Creep-fatigue test with initial compression is compared with that with initial tension: (a) and (b) the time evolution of σ_n and ρ for the test condition of t_t=100 s, t_c=20 s (i.e. t_t>t_c); (c) and (d) the time evolution of σ_n and ρ for the test condition of t_t=20 s, t_c=100 s (i.e. t_t<t_c)

Fig. 6d depicts the time evolution of ρ curves for these two test conditions. After each cycle, the ρ curves drop to 0, indicating that all of the cavities nucleated in the tension phase are sintered during the subsequent long compressive hold (t_c=100 s). By comparison of Fig. 6b with 6d, it can be known that the nucleation rate in the tests with t_c=100 s is almost ten orders of magnitude higher than that in the tests with t_c=20 s. This is due to the fact that the maximum σ_n is higher in the test with t_c=100 s (1043 MPa in Fig.6a) when compared with that test with t_c=20 s (761 MPa in Fig.6c). However, this does not necessarily lead to the overall increase of cavitation damage as the prolonged compressive hold would also cause sintering and close all cavities nucleated in the previous tension phase.

3.3 Combined effect of tensile and compressive holds

Combined effect of t_t and t_c on the final ρ after 10 cycles is presented in Fig. 7a by the contour plot. Note that except for the t_t and t_c, the default value as given in Table 2 is used for all the other load-waveform parameters and temperature. The contour curves of 0.1 and 0.0001 in Fig. 7a are very close to each other, suggesting that the contour curve of 0.1 can be used as the lower bound value. In other words, below this value, the final ρ is negligible. There is a threshold value of t_t for cavitation when t_c=0 s, indicating that the nucleated cavities can be sintered by the load reversal from tension to compression. In addition, under the condition of t_c=0 s, the contour curves with values of 0.5 and beyond do not intercept with the x-axis. This indicates that there is an upper bound value for t_t; any prolonged tensile hold t_t than this critical value would not further contributing to the final ρ. This is probably attributed to the rapid decrease of σ_n during tensile hold as informed by the exponential decay function in Eq.(2).

Now let's focus on the changing values of t_c. When t_t is less than 60 s, increasing t_c helps to reduce the final ρ. But when t_t is greater than 60 s, an increased t_c promotes the increased final ρ until reaching the allowable value as highlighted by the magenta dash curve in Fig. 7a. It is also evident that the allowable t

$_{\mathrm{c}}$ increases with the increasing t_{t}. The presence of allowable t_{c} is the result of two competing effects: (i) the increased t_{c} can promote the cavity nucleation rate by affecting the maximum σ_{n} in the next tension phase; (ii) the prolonged t_{c} increases the likelihood of cavity sintering process, given the compressive stress.

Furthermore, the combined effect of t_{t} and t_{c} on the final f is presented in Fig. 7b. The distribution of contour curves looks similar by the comparison of Fig. 7a with 7b, suggesting that the dependence of final ρ and f on the load waveform parameters are highly consistent, i.e. both are positively correlated with the maximum σ_{n}.

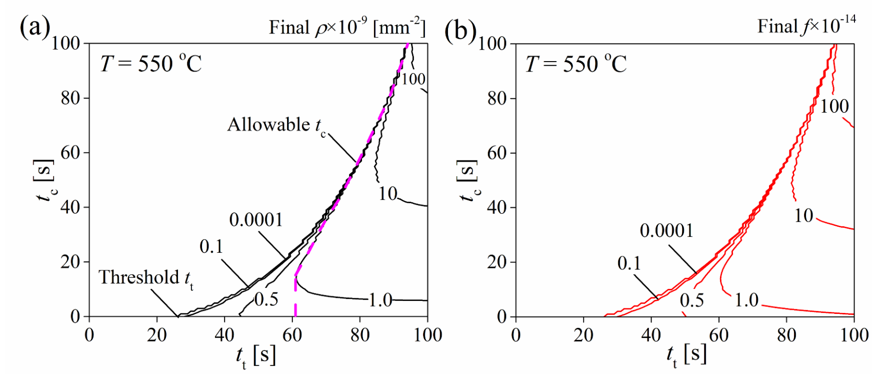

Fig. 7: Dependences of the cavity number density ρ after 10 cycles in (a) and the cavitated GB area fraction f in (b) on the tensile and compressive hold times of t_{t} and t_{c}

3.4 Effect of stress magnitude in tensile and compressive holds

Fig. 8a presents the effect of $\Delta\sigma_{\mathrm{t}}$ on final ρ (i.e. calculated after 10 cycles); the values of $\Delta\sigma_{\mathrm{t}}$ and t_{t} are varied for this purpose. Other input parameters are kept the same as those listed in Table 2. A positive correlation is found between ρ and $\Delta\sigma_{\mathrm{t}}$ for both t_{t}=100 s and 60 s, suggesting that a higher tensile stress promotes a higher cavity nucleation rate. However, the breakdown of this correlation occurs when $\Delta\sigma_{\mathrm{t}}$ is lower than ~145 MPa under the condition of t_{t}=60 s. This sharp decrease in final ρ is related to the effect of compression phase on cavity sintering. When the tensile stress reduces to lower level, the associated σ_{n} under a fixed t_{t} does not allow the nucleated cavities to grow large enough to be survived from the following compression phase where the sintering would occur. As shown in the enlarged view of Fig. 8a, such a threshold $\Delta\sigma_{\mathrm{t}}$ appears at the stress level of ~105 MPa under the condition of t_{t}=100 s. This means that the threshold value for $\Delta\sigma_{\mathrm{t}}$ to generate the cavitation is inversely proportional to t_{t} (i.e. 145 MPa for t_{t}=60 s as compared with 105 MPa for t_{t}=100 s)

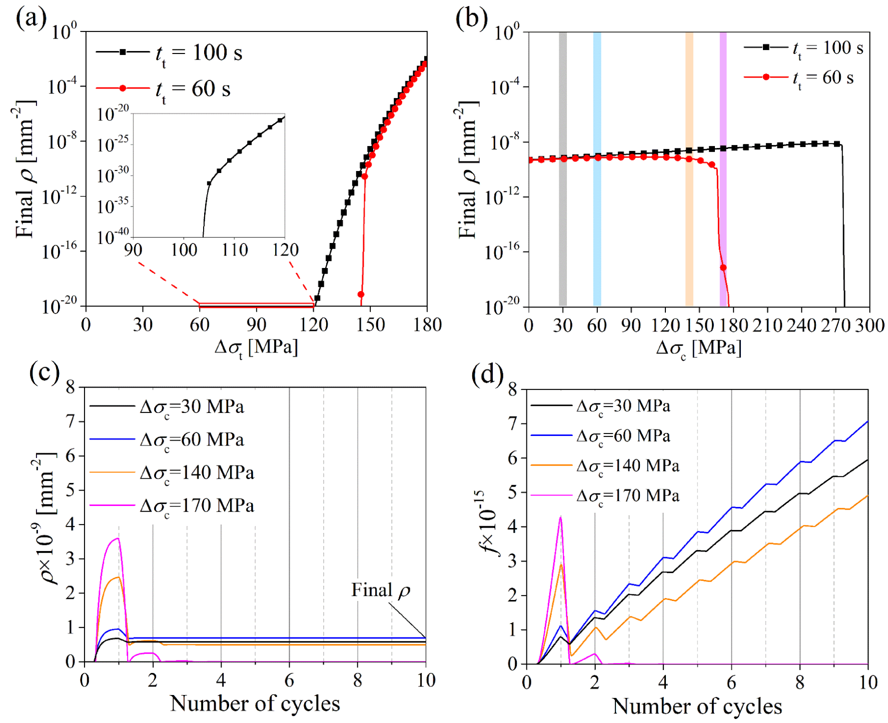

Fig. 8: The dependence of final ρ on (a) $\Delta\sigma_t$ and (b) $\Delta\sigma_c$ with t_t= 60/100 s; the evolution of ρ in (c) and f in (d) as a function of fatigue cycles calculated with different stress magnitudes of $\Delta\sigma_c$=30/60/140/170 MPa but under the same tensile hold time of t_t=60 s.

In terms of the effect of $\Delta\sigma_c$ on the final ρ , a positive correlation is found between the two until $\Delta\sigma_c$ reaching the breakdown value, Fig. 8b. Such breakdown of the positive correlation can be seen when $\Delta\sigma_c$>120 MPa under the condition of t_t=60 s. This is followed by a sharp drop of final ρ when $\Delta\sigma_c$>160 MPa. With the increase of tensile hold time to t_t=100 s, the breakdown occurs at a higher compressive stress of when $\Delta\sigma_c$>270 MPa.

To explain this interesting phenomenon, the change of ρ and f as a function of cycles are presented in Fig. 8c and 8d, respectively. Four different stress levels of $\Delta\sigma_c$=30/60/140/170 MPa are considered, and they represent different characteristic regions as highlighted by using different colours in Fig. 8b. Comparing the values of ρ at the end of the 1st cycle, the test with $\Delta\sigma_c$=170 MPa has the largest ρ of 3.6×10^{-9}mm^{-2}, whereas that with $\Delta\sigma_c$=30 MPa shows the smallest ρ of 0.7×10^{-9}mm^{-2}, Fig. 8c. This indicates that a higher $\Delta\sigma_c$ helps to produce more creep cavities in the subsequent tension phase. However, in the next compression phase of the 2nd cycle, these nucleated cavities would be sintered to different extents depending on the stress level of $\Delta\sigma_c$. For example, the ρ value reduction is found to be -0.2×10^{-9}, -0.3×10^{-9}, -1.9×10^{-9} and -3.6×10^{-9}mm^{-2} for $\Delta\sigma_c$=30, 60, 140 and 170 MPa, respectively, Fig. 8c. Thus, the competing effect of $\Delta\sigma_c$ on ρ through the cavity nucleation and sintering leads to the fact that an intermediate level of $\Delta\sigma_c$ is more likely to create more cavities.

For the same reason, the breakdown of the positive correlation between the final ρ and $\Delta\sigma_c$ as revealed in Fig. 8b, can be explained by the sintering effect that becomes predominant when the compressive stress is sufficiently large. In terms of the cavitated GB fraction f , its value increases with the number of cycles, Fig. 8d. The zigzag shape in the f curves reflect the alternating nucleation and sintering events. In summary, increasing the stress level of $\Delta\sigma_t$ is more effective in enhancing the final ρ when compared to $\Delta\sigma_c$. The underlying mechanism is the side effect associated with the cavity sintering due to the increased $\Delta\sigma_c$.

3.5 Effect of stress variation rate

After elaborating the effects of four input parameters (t_{t}, t_{c}, $\Delta\sigma_{\mathrm{t}}$ and $\Delta\sigma_{\mathrm{c}}$), we now consider the effect of stress variation rate , Fig. 4. To limit the effect of hold time on the prediction results, botht_{c} and t_{t} are set to 0 s for calculations. Fig. 9a shows the effect of on the final ρ and$f$ after 10 cycles. There is an optimum value of (˜0.4 MPa/s) that leads to the maximum final $\rho$and f . To explain its presence, the ρ values as calculated at the end of 1st cycle (i.e. the moment of finishing the tension phase) are presented in Fig. 9b, while the minimum σ_{n} as calculated in the 2nd cycle (i.e. the following compression phase) are shown in Fig. 9c. Note that the magnitude of ρ at the end of 1st cycle can be regarded as the evaluation of the nucleation ability in the considered load-waveform shape. Equally, the absolute value of the minimum σ_{n} in the 2nd cycle can be regarded as the evaluation of the sintering ability.

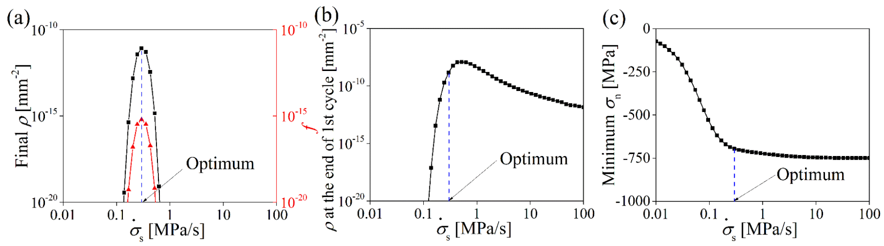

Fig. 9: (a) Dependence of final ρ and f on stress variation rate under t_{c} andt_{t}=0 s; (b) ρ value at the end of 1st cycle and (c) the related minimum σ_{n} in the compression phase of 2nd cycle.

Fig. 9b shows that ρ decreases rapidly with the decrease of in the range of <0.4 MPa/s. This implies that a too low stress variation rate reduces the nucleation ability. This seems to agree with the previous one-cycle creep-fatigue modelling work[19], where the local normal stress relaxation was found to occur during the load reversal with low . On the other hand, theρ curve decreases with the increase of when >0.4 MPa/s. At first glance, this might be attributed to the lack of nucleation time when becomes sufficiently high. However, a closer examination of the change of final ρ in Fig. 9a in comparison with the ρ curve in Fig. 9b does not support the above explanation. It is evident that the final ρ quickly decreases to a value of 10^{-20} mm^{-2} with increased , Fig. 9a, whereas the ρ at the end of 1st cycle decreases moderately to 10^{-12} mm^{-2}, Fig. 9b.

We thereby hypothesised that the enhanced cavity sintering effect contributed to the rapid decrease in the high range. Fig. 9c shows that the absolute value of the minimum σ_{n} has a monotonically increasing trend with the increase of . This suggests that the sintering effect becomes more pronounced in the high range, causing the final ρ to decrease, as revealed in Fig. 9a. To this end, our hypothesis is supported by the observation.

Finally, it can be seen in Fig. 9b that the optimum does not coincide with the value of producing the maximum ρ value. It is the combined effect of sintering and nucleation over the course of 10 cycles that determines the optimum value leading to the highest final ρin Fig. 9a (for brevity not shown here).

4. Model applications

4.1 Nucleation incubation time

An incubation time is required to nucleate cavities [5]. The underlying mechanism is the time consumed for vacancies gathering into the nuclei to form a stable cavity [40]. In our model predictions, there is a threshold value oft_{t} for creep-fatigue tests without applying compressive stress hold (t_{c}=0 s), Fig. 7a. This can be considered as the equivalent nucleation incubation time. Fig. 10 presents the calculated values for Type 316 stainless steel under compressive/tensile stresses of (in MPa): -150/+150, -100/+150, and -150/+100 at different temperatures. The increase of temperature by 50 @C reduces the incubation time more than one-half. This agrees with the experimental data trend on dispersion-strengthened copper alloy between 700 and 800 @C [41]. If we take the prediction curve of -150/+150 MPa as the comparison reference, decreasing the tensile stress by 50 MPa results in doubling the incubation time, Fig. 10. On the other hand, the incubation time is shortened by 25%, when the compressive stress is decreased by 50 MPa.

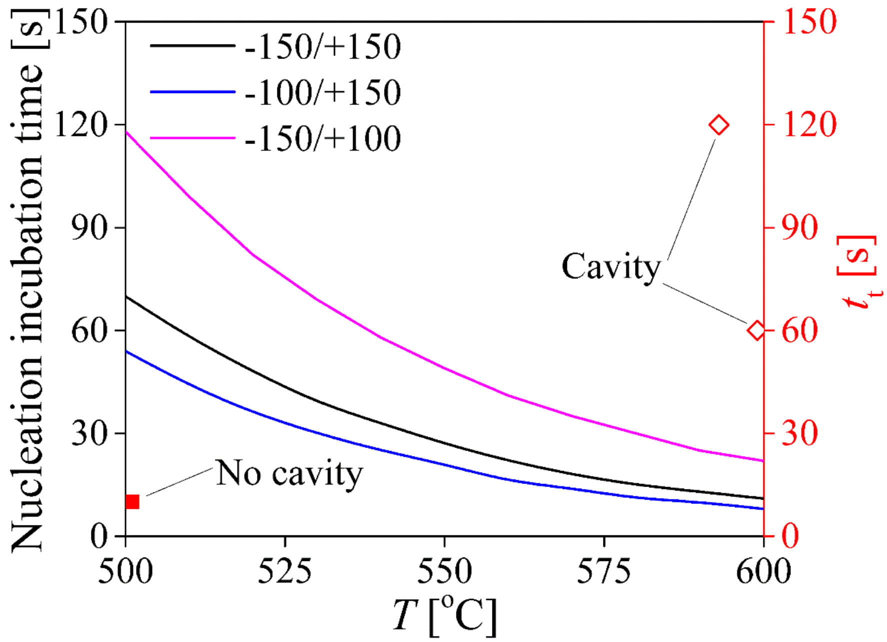

Fig. 10: Model predicted nucleation incubation time (with stress amplitude and temperature indicated) in comparison with experimental data. Experimental data points are collected from creep-fatigue tests on Type 316 stainless steel.

Overall, our cavitation model informs that temperature and tensile stress are two influencing factors for the nucleation incubation time. For comparison purposes, experimental results are plotted as red data points in Fig. 10. The 'no cavity' data was obtained from the work by Shi and Pluvinage [42]. The creep-fatigue test was conducted at 500 @C on Type 316L stainless steel under total strain range of 1.60% (stress amplitude of 350 MPa) together with tensile hold of t_t=10 s. They observed no creep cavitation damage, being consistent with the transgranular crack propagation mode. In addition, the 600 @C 'cavity' data point was obtained from the creep-fatigue test on Type 316 stainless steel conducted by Hales[43]. They found cavitation damage under the test condition of total strain range of 0.5% and t_t=60 s. No stress-strain hysteresis loop was given, and hence the stress amplitude has been calculated as 140 MPa using relevant database in [38]. The 593 @C 'cavity' data point was obtained from the creep-fatigue crack growth test on Type 316 stainless steel conducted by Michel and Smith [44]. The test was performed with the initial stress intensity factor range of 20 MPa.m^{-2}, and they reported the presence of intergranular creep damage. In summary, our model prediction agrees with the experimental observation.

4.2 Cycle frequency range

Cavitation can also be found in high-temperature fatigue tests under certain range of cycle frequencies [45]. The cycle frequency that is positively correlated with the stress variation rate can be defined as . The optimum for final ρ has been calculated under the condition of without stress hold (i.e. t_c and t_t=0 s indicative of pure fatigue) has been presented in Fig. 9a. Hence, it is possible to extend our model prediction to examine the nucleation ability under different cycle frequency range for high-temperature fatigue.

The frequency range for cavity nucleation depends on both the temperature and stress amplitude. Fig. 11 presents the predicted nucleation field in the stress amplitude and frequency space at 550 and 600 @C. Here, the nucleation criterion is defined as the final $\rho$of [?]10^{-20} mm^{-2}. In other words, if the condition of $\rho < 10^{-20} mm^{-2}$ is met, the combination of stress amplitude and frequency is judged as being unable to create cavitation. The shape of the nucleation field looks like the upside-down hills. This means that the load waveform with a higher stress amplitude has a wider range of cycle frequencies to promote cavitation. Also, an optimum frequency is found at each temperature, allowing the lowest stress amplitude to meet the cavitation criterion. The presence of optimum frequency shares the same mechanism as the optimum in Fig. 9. In low frequency, the lack of nucleation ability is the reason, whereas enhanced sintering is responsible for the reduced cavities in the high frequency.

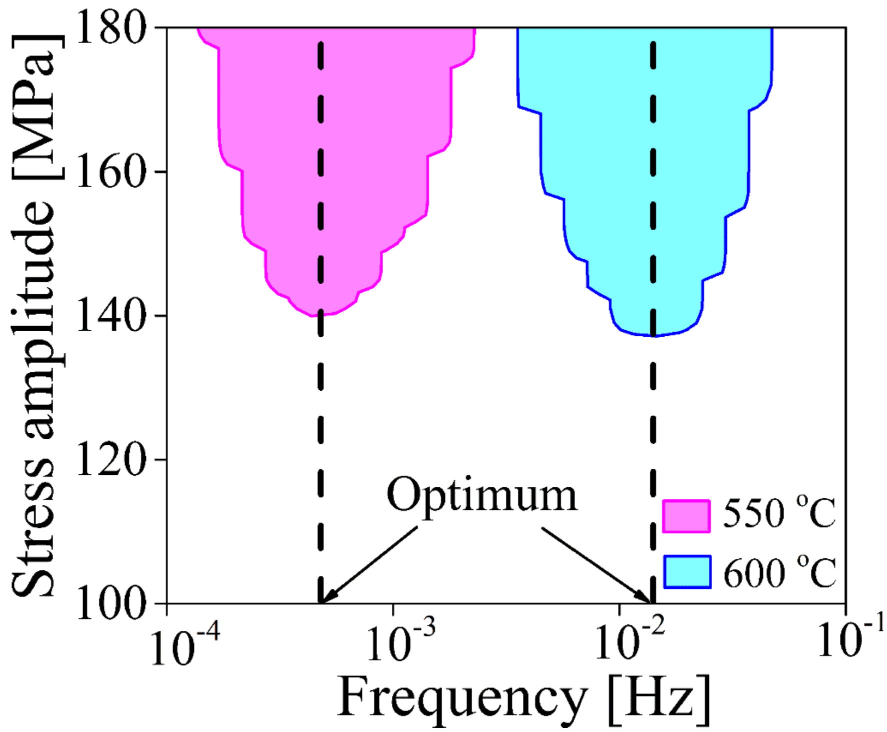

Fig. 11: Model predicted cavity nucleation field in stress amplitude and frequency space for Type 316 stainless steel at 550 and 600 @C.

It is also interesting to note that the optimum frequency and the whole frequency range are positively correlated with temperature, Fig. 11. This can be explained by the time constant τ, Eq.. τ is inversely proportional to temperature, given that k_e is temperature independent but both the η_b and are inversely proportional to temperature. As commented in[18], a lower τ means that a higher stress variation rate would be required to achieve the same level ofσ_n leading to cavitation. Therefore, the nucleation frequency increases with the temperature (i.e. decreasing τ).

Taplin, Tang [46] and Tang, Taplin [47]developed a mechanism map for cavity nucleation in the stress amplitude and frequency space. For GB sliding induced cavitation, their predicted nucleation frequency for Type 304 stainless steel was in the range from 3×10^{-2} to 1 Hz under stress amplitude of 180 MPa, and 3×10^{-2} to 5×10^{-1} Hz under stress amplitude of 140 MPa, respectively. This agrees with our model prediction in a sense that a higher stress amplitude leads to a wider range of nucleation frequencies. Also, the frequency ranges obtained at 650 @C in their predictions are generally higher than our model predictions at 600 @C (3×10^{-3} to 5×10^{-2} Hz), Fig. 11. Thus, our model prediction successfully captures the positive correlation between the nucleation cycle frequency and temperature.

4.3 Unequal ramp rate

In the past two decades, high-temperature fatigue testing with unequal ramp rate has emerged as alternative method to study cavitation damage during creep-fatigue interaction, as demonstrated in[5]. Yamaguchi and Kanazawa [48] studied effects of unequal ramp rate on the strain-controlled high-temperature fatigue in Type 316 stainless steel at 600 @C. It was found that the test with a slow-fast cycling waveform exhibited an intergranular fracture mode, and the fatigue life was reduced significantly due to creep cavitation. By comparison, the test with a fast-slow waveform fractured in a transgranular manner, and limited fatigue life reduction was found.

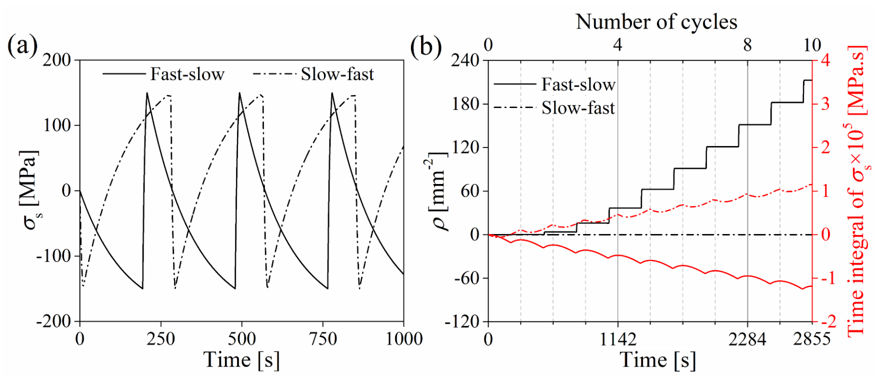

Fig. 12: (a) Applied stress as a function of time for the fast-slow and slow-fast creep-fatigue load waveforms; (b) predicted time evolution ofρ and the time integral of σ_s at 600 @C.

Now let's consider the unequal ramp rate scenarios from the modelling perspective. Fig. 12a presents the time-evolution curves ofσ_s for both the fast-slow and slow-fast cycling, and they were used as the model input. The corresponding ρ curves in black are shown in Fig. 12b. It can be seen that the ρ in fast-slow test gradually increases after a few cycles, whereas that of the slow-fast test accumulates negligible number of cavities. This is in conflict with the experimental results as the failure of slow-fast test was dominated by creep cavitation. To reconcile this seemingly contradictory phenomenon, it is important to recollect the concept of our cavity nucleation and early-stage growth model.

Schematic diagram in Fig. 13 depicts the whole process of creep cavitation. The respective nucleation and subsequent early-stage growth in Fig. 13a and 13b are the main focus of the present work. Since the nucleated cavities are extremely small (<0.1 µm) compared with the particles at GB, they are surrounded by a highly localised and time-dependent stress field σ_n, induced by the GB sliding with the rate of , Fig. 13b. However, the growth mechanism of large sized cavities would be completely different. Fig. 13c shows that the large cavity is surrounded by a uniform stress field under the far-field stress σ_s. The cavity coalescence shown in Fig. 13d is also affected by the stress concentration, but this stress concentration is due to the reduction in effective load-bearing area [49], which approximately equals$\sigma_s/(1\text{-}f)$ [50]. Therefore, it can be considered that the local normal stressσ_n is key to early-stage creep cavitation, whereas the far-field stress σ_s controls its late-stage.

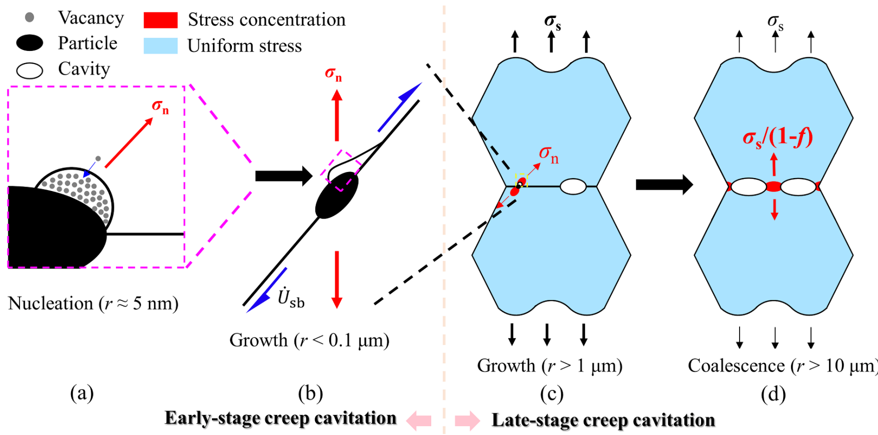

Fig. 13. A schematic diagram of cavitation with particular emphasis on the difference between early- and late-stage cavity growth: (a) nucleation; (b) early-stage; (c) late-stage and (d) coalescence.

In the late-stage cavitation, damage increase is manifested by the radius increase of large sized cavities. According to the traditional growth model, the growth rate is positively correlated with the cavity radius [24, 51, 52]. Also, the late-stage growth rate is controlled by applied stress σ_s. Therefore, the time integral of σ_s can be used to assess the propensity of late-stage growth under a given load-waveform shape. In this sense, a positive value of the integral ofσ_s indicates that the cavities would continue growing up, whereas a negative value indicating shrinkage in size. Bearing the difference between the early- and late-stage in mind, theρ curves in Fig. 12b for the fast-slow and slow-fast load-waveforms can be reconciled as below.

The time integral of σ_s (red curves) for the two scenarios are superimposed in Fig. 12b with their values indicated by the secondary y-axis. The slow-fast one shows a positive value of theσ_s integral, whereas the fast-slow one shows a negative value. This implies that cavities in the case of fast-slow is difficult to grow up under the negative value ofσ_s integral. By contrast, cavities formed in the slow-fast cycling is more likely to continue growing up, although their number density is much less compared to that in the fast-slow one. This eventually leads to an increased cavitated GB fraction f in the case of slow-fast. The cavity coalescence occurs when f becomes sufficiently large, causing the formation of intergranular cracks in macroscopic scale. Hence, cavitation associated intergranular fracture was most likely to occur in the case of slow-fast compared to the fast-slow, as experimentally observed in [5, 48].

5. Conclusions

A mechanistic based cavitation model that considers nucleation, early-stage growth and sintering under multi-cycle creep-fatigue interaction has been developed to provide predictions of both the number density of cavities and the area fraction of cavitated grain boundaries in Type 316 stainless steel. The model replies on the local normal stress to connect the three concurrent or sequential cavitation events, providing important insights about how to design the creep-fatigue load waveform so that the creep cavitation can be enhanced. The following conclusions can be reached:

1. When tensile hold time is longer than that of compression, the creep-fatigue test with initial compression is advantageous in terms of creating more cavities.
2. Unbalanced stress hold time in favour of compression most likely closes all of the cavities nucleated during the previous tension phase.
3. Effect of compressive hold time or stress level on the number density of cavities in creep-fatigue tests is not monotonic. The underlying mechanism is their competing effect on nucleation and sintering.

4. There is an optimum value for the stress variation rate to obtain the highest number density of cavities, and their presence can be attributed to sintering effect.
5. Our model can satisfactorily explain several interesting experimental observations, including nucleation incubation time, effective nucleation field in a stress-frequency space for high-temperature fatigue, and the effect of unequal ramp rate on cavitation.

Acknowledges

Bo Chen acknowledges financial supports by the UK's Engineering and Physical Sciences Research Council, EPSRC Early Career Fellowship Scheme [EP/R043973/1] as well as East China University of Science and Technology through the Ministry of Education of the People's Republic of China 'the 111 Project'. Jingdong Hu is funded partly by China Scholarship Council (CSC) [No.201906740075] through the PhD Exchange Scheme. Bo Chen extends his sincere gratitude to Prof Shan-Tung Tu for providing academic mentorship and endless support.

Appendix A. Equations for deriving the local normal stress in Eq.

To derive Eq.(2) for the local normal stress σ_n, let's consider the 'spring-dashpot' framework adopted in the Chen-Hu model [19], Fig. A1. The left arm describes the stress applied on a grain boundary (GB), and the right arm describes the stress applied on the neighbouring grains.

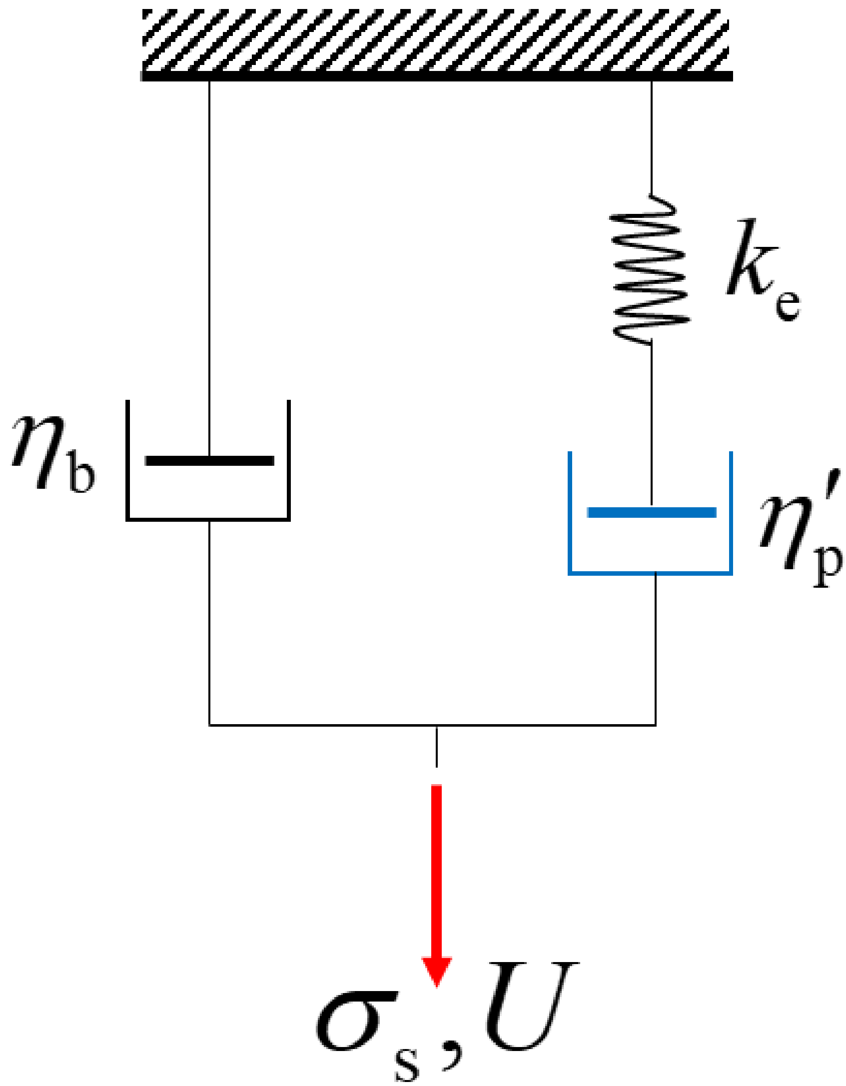

Fig. A1 Spring-dashpot model [19]

The local normal stress σ_n is equivalent to the stress concentration at GB particles, which gives:

where is the GB sliding rate. η_p is damping coefficient for the Norton power-law creep with the deformation rate as formulised below:

where σ_{sa} is the stress shared in the neighbouring grains. An intermediate parameter, transient damping coefficient , has been introduced to reduce the complexity when calculating the . Then, at the next time $t + \Delta t$ can be calculated by $\sigma_s(t + \Delta t)$ and$\sigma_n(t)$ from previous time t :

For a sufficiently small time increment Δt , can be approximated as a constant. Thus, the differential equation forσ_n can be derived as:

Basically, Eq. is the solution of Eq., and that explicit form is more convenient for numerical calculations.

Appendix B. Surface diffusion factor D_S and the derivation of Eq.(4)

Free surface diffusion coefficient D_S is used only in Eq.(4) to describe the crack-like cavity growth rate via the diffusivity ratio of $\delta_S D_S/\delta\Delta_B$=0.001. The condition that determines the low or high stress, as reported in[34], is formulised as:

A sensitivity study was conducted at 550 @C to examine the effect of the $\delta_S D_S/\delta\Delta_B$ value selection on the cavity growth rate. Fig. B1 shows the calculated relationship between the local normal stress σ_n and cavity growth rate by using different $\delta_S D_S/\delta\Delta_B$ values. Only the $\delta_S D_S/\delta\Delta_B$ values of less than 1 need to be considered for the crack-like cavity growth [34]. Within the stress range of 100 to 1000 MPa, the calculated curve with $\delta_S D_S/\delta\Delta_B$=0.001 (in red) shows the highest cavity growth rate, Fig. B1. The solid curves as predicted using Eq. are not continuous. A modification was made to the function (see Eq.), to provide a continuous curve prediction (the dashed curve). The stress range highlighted by red box indicates the magnitude facilitating the cavity growth, according to Figs. 5 and 6. For the maximum cavitation under creep-fatigue, $\delta_S D_S/\delta\Delta_B$=0.001 has thus been selected to derive the value of D_S.

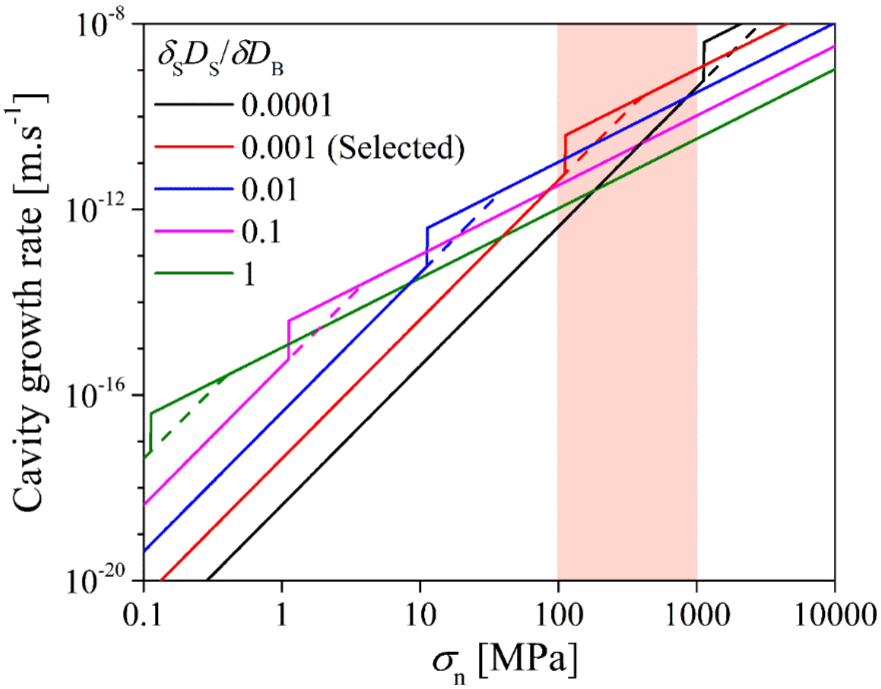

Fig. B1 Effect of diffusivity ratio $\delta_S D_S/\delta\Delta_B$ on the cavity growth rate. Dashed curves were predictions using Eq., while solid curves were based on Eq..

Appendix C. Numerical error

The forward Euler method creates a limited numerical calculation error, if the time interval Δt is small enough. This method has been used in previous work on cavitation, e.g. Sanders, Dadfarnia[52], Margolin, Gulenko [53]. Fig. C1 presents calculation results on the basis of different Δt values. It is clear that Δt =0.5

s generates a marginal difference (less than 2.5%) when compared with those using any smaller values (e.g. Δt =0.1, 0.05 s). Thus the selection of Δt =0.5 is justified.

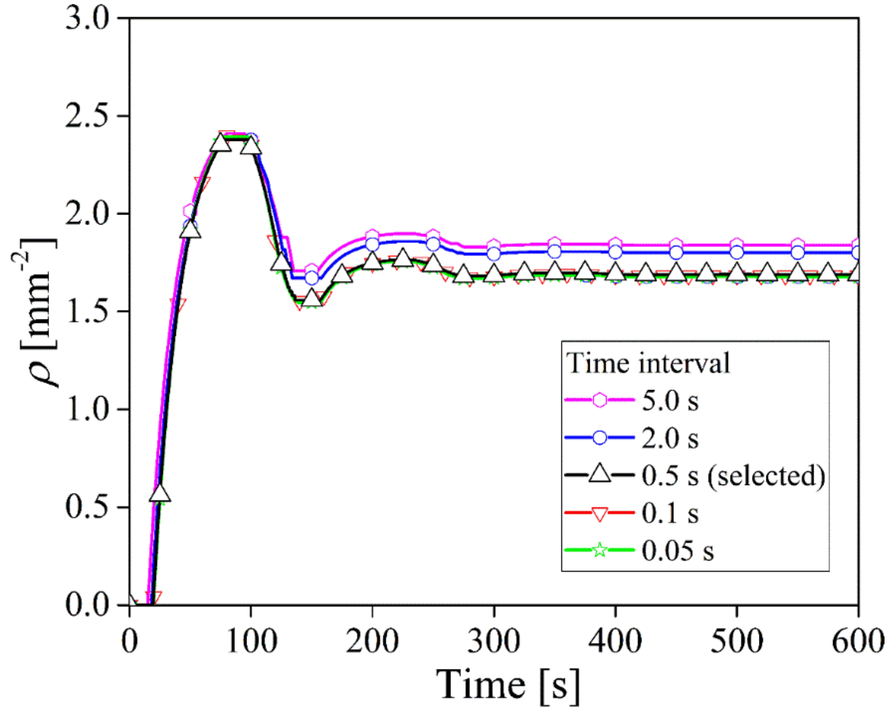

Fig. C1 Effect of Δt value on the numerical calculation results Δt =0.5, under the condition of 550 @C, stress amplitude of 200 MPa with initial tension, zero mean stress, and tensile hold time of 60 s.

Reference

1. Hales R (1980) A quantitative metallographic assessment of structural degradation of type 316 stainless steel during creep-fatigue.*Fatigue & Fracture of Engineering Materials & Structures* .**3** : 339-356.

2. Murty KL, Charit I (2008) Structural materials for Gen-IV nuclear reactors: Challenges and opportunities. *Journal of Nuclear Materials* . **383** : 189-195.

3. Kassner ME, Hayes TA (2003) Creep cavitation in metals.*International Journal of Plasticity* . **19** : 1715-1748.

4. Skelton RP, Gandy D (2008) Creep–fatigue damage accumulation and interaction diagram based on metallographic interpretation of mechanisms. *Materials at High Temperatures* . **25** : 27-54.

5. Rodriguez P, Rao KBS (1993) Nucleation and growth of cracks and cavities under creep-fatigue interaction. *Progress in Materials Science* . **37** : 403-480.

6. Davanas K (2020) Determination of creep cavity nucleation rates.*Materials at High Temperatures* . **37** : 75-80.

7. Nam SW (2002) Assessment of damage and life prediction of austenitic stainless steel under high temperature creep-fatigue interaction condition. *Materials Science and Engineering A* . **322** : 64-72.

8. Cailletaud G, Nouailhas D, Grattier J, et al. (1984) A review of creep-fatigue life prediction methods: identification and extrapolation to long term and low strain cyclic loading. *Nuclear engineering and design* . **83** : 267-278.

9. Wen J-F, Srivastava A, Benzerga A, Tu S-T, Needleman A (2017) Creep crack growth by grain boundary cavitation under monotonic and cyclic loading. *Journal of the Mechanics and Physics of Solids* .**108** : 68-84.

10. Barbera D, Chen H, Liu Y (2017) Advances on creep–fatigue damage assessment in notched components. *Fatigue & Fracture of Engineering Materials & Structures* . **40** : 1854–1867.

11. Wilkinson DS (1978) The Mechanisms of Pressure sintering. University of Cambridge.

12. Stevens RA, Flewitt PEJ (1983) The sintering of creep-induced cavities in a low alloy ferritic steel (1Cr1Mo0.75V).*Metallurgical Transactions A* . **14** : 679-686.

13. Greenwood JN (1952) Intercrystalline cracking of metals.*Journal of the Iron and Steel Institute* . **171** : 380-380.

14. Raj R, Ashby MF (1975) Integranular fracture at elevated temperature. *Acta Metallurgica* . **23** : 653-666.

15. Evans HE (1984) *Mechanisms of creep fracture* . Elsevier Applied Science, Essex, UK, 319.

16. Chen CW, Machlin ES (1957) On a mechanism of high temperature intercrystalline cracking. *JOM* . **9** : 829-835.

17. Dunand DC, Han BQ, Jansen AM (1999) Monkman-grant analysis of creep fracture in dispersion-strengthened and particulate-reinforced aluminum.*Metallurgical and Materials Transactions A* . **30** : 829-838.

18. Min BK, Raj R (1978) Hold-time effects in high-temperature fatigue.*Acta Metallurgica* . **26** : 1007-1022.

19. Hu J-D, Xuan F-Z, Liu C-J, Chen B (2021) Modelling of Cavity Nucleation under Creep-fatigue Interaction. *Mechanics of Materials* . **156** : 103799.

20. Cocks ACF (1989) Inelastic deformation of porous materials.*Journal of the Mechanics and Physics of Solids* . **37** : 693-715.

21. Cocks ACF, Ashby MF (1982) Creep fracture by coupled power-law creep and diffusion under multiaxial stress. *Metal Science* .**16** : 465-474.

22. Needleman A, Rice JR (1980) Plastic creep flow effects in the diffusive cavitation of grain boundaries. *Acta Metallurgica* .**28** : 1315-1332.

23. Chuang T-J, Kagawa KI, Rice JR, Sills LB (1979) Non-equlibrium models for diffusive cavitation of grain interfaces. *Acta Metallurgica* . **27** : 265-284.

24. Chen I-W, Argon AS (1981) Diffusive growth of grain-boundary cavities. *Acta Metallurgica* . **29** : 1759-1768.

25. Chen I-W (1983) Mechanisms of cavity growth in creep. *Scripta Metallurgica* . **17** : 17-22.

26. Miller DA, Hamm CD, Phillips JL (1982) A mechanistic approach to the prediction of creep-dominated failure during simultaneous creep-fatigue.*Materials Science and Engineering* . **53** : 233-244.

27. Tahir F, Liu Y (2017) A new experimental testing method for investigation of creep-dominant creep-fatigue interaction in Alloy 617 at 950 °C. *International Journal of Pressure Vessels and Piping* .**154** : 75-82.

28. Fournier B, Sauzay M, Caes C, et al. (2008) Creep–fatigue–oxidation interactions in a 9Cr–1Mo martensitic steel. Part I: Effect of tensile holding period on fatigue lifetime.*International Journal of Fatigue* . **30** : 649-662.

29. Chen B, Flewitt PEJ, Cocks ACF, Smith DJ (2015) A review of the changes of internal state related to high temperature creep of polycrystalline metals and alloys. *International Materials Reviews* . **60** : 1-29.

30. Frost HJ, Ashby MF (1982) *Deformation Mechanism Maps: The Plasticity and Creep of Metals and Ceramics* . Pergamon Press, Oxford, UK.

31. Mortimer DA, Nicholas MG (1976) Surface and grain-boundary energies of AISI 316 stainless steel in the presence of boron. *Metal Science* . **10** : 326-332.

32. Wang JS, Stephens JJ, Nix WD (1985) A statistical analysis of cavity nucleation at particles in grain boundaries. *Acta Metallurgica* .**33** : 1009-1021.

33. Stroh AN (1957) A theory of the fracture of metals. *Advances in Physics* . **6** : 418-465.

34. Nix WD, Yu KS, Wang JS (1983) The effects of segregation on the kinetics of intergranular cavity under creep conditions.*Metallurgical Transactions A* . **14** : 563-570.

35. Riedel H (1987) *Fracture at high temperatures* . Springer, Berlin, Heidelberg.

36. Fedelich B, Owen J (2009) Creep damage by multiple cavity growth controlled by grain boundary diffusion. *12th International Conference on Fracture* , Ottawa, Canada.

37. Chen B, Hu JN, Flewitt PEJ, et al. (2015) Effect of thermal ageing on creep and oxidation behaviour of Type 316H stainless steel.*Materials at High Temperatures* . **32** : 592-606.

38. ASME (2015) ASME BPVC III-Div.1 Subsection NH. *Class 1 Components in Elevated Temperature Ser vice* . ASME, New York.

39. Chen B, Flewitt PEJ, Smith DJ, Jones CP (2011) An improved method to identify grain boundary creep cavitation in 316H austenitic stainless steel. *Ultramicroscopy* . **111** : 309-313.

40. Raj R (1978) Nucleation of cavities at second phase particles in grain boundaries. *Acta Metallurgica* . **26** : 995-1006.

41. Fleck RG, Taplin DMR, Beevers CJ (1975) An investigation of the nucleation of creep cavities by 1 MV electron microscopy. *Acta Metallurgica* . **23** : 415-424.

42. Shi HJ, Pluvinage G (1994) Cyclic stress-strain response during isothermal and thermomechanical fatigue. *International Journal of Fatigue* . **16** : 549-557.

43. Hales R (1980) A quantitative metallographic assessment of structural degradation of type 316 stainless steel during creep-fatigue.*Fatigue & Fracture of Engineering Materials & Structures* .**3** : 339-356.

44. Michel DJ, Smith HH (1980) Accelerated creep-fatigue crack propagation in thermally aged type 316 stainless steel. *Acta Metallurgica* . **28** : 999-1007.

45. Ghafouri SN, Faulkner RG, Chung TE (1986) Microstructural developments in type 316L stainless steel during low-cycle fatigue at 350–550degC and their effects on cyclic strength and life.*Materials Science and Technology* . **2** : 1223-1232.

46. Taplin DMR, Tang NY, Leipholz HHE (1984) On fatigue-creep-environment interaction and the feasibility of fatigue maps. *6th International Conference on Fracture* . Elsevier, New Delhi, India, 127-142.

47. Tang NY, Taplin DMR, Plumtree A (1985) Schema for depicting cavity nucleation during hightemperature fatigue. *Materials Science and Technology* . **1** : 145-151.

48. Yamaguchi K, Kanazawa K (1980) Effect of strain wave shape on high temperature fatigue life of a type 316 steel and application of the strain range partitioning method. *Metallurgical Transactions A* .**11** : 2019-2027.

49. Morin L, Leblond J-B, Benzerga AA, Kondo D (2016) A unified criterion for the growth and coalescence of microvoids. *Journal of the Mechanics and Physics of Solids* . **97** : 19-36.

50. Cocks ACF, Ashby MF (1980) Intergranular fracture during power-law creep under multiaxial stresses. *Metal Science* . **14** : 395-402.

51. Hu J-D, Xuan F-Z, Liu C-J (2018) A void growth model of multiaxial power-law creep rupture involving the void shape changes.*International Journal of Mechanical Sciences* . **144** : 723-730.

52. Sanders JW, Dadfarnia M, Stubbins J, Sofronis P (2017) On the fracture of high temperature alloys by creep cavitation under uniaxial or biaxial stress states. *Journal of the Mechanics and Physics of Solids* . **98** : 49–62.

53. Margolin BZ, Gulenko AG, Kursevich IP, Buchatskii AA (2006) Modeling for fracture in materials under long-term static creep loading and neutron irradiation. Part 1. A physico-mechanical model. *Strength of Materials* . **38** : 221-233.